

**Electronic, optical, and structural properties of (In,Ga)As/GaP quantum dots**C. Robert,<sup>1,\*</sup> C. Cornet,<sup>1</sup> P. Turban,<sup>2</sup> T. Nguyen Thanh,<sup>1</sup> M. O. Nestoklon,<sup>4</sup> J. Even,<sup>1</sup> J. M. Jancu,<sup>1</sup> M. Perrin,<sup>1</sup> H. Folliot,<sup>1</sup> T. Rohel,<sup>1</sup> S. Tricot,<sup>2</sup> A. Balocchi,<sup>3</sup> D. Lagarde,<sup>3</sup> X. Marie,<sup>3</sup> N. Bertru,<sup>1</sup> O. Durand,<sup>1</sup> and A. Le Corre<sup>1</sup><sup>1</sup>Université Européenne de Bretagne, INSA, FOTON, UMR 6082, F-35708 Rennes, France<sup>2</sup>Equipe de Physique des Surfaces et Interfaces, Institut de Physique de Rennes UMR URI-CNRS 6251, Université de Rennes 1, F-35042 Rennes Cedex, France<sup>3</sup>Université de Toulouse, INSA-CNRS-UPS, LPCNO, 135 avenue de Rangueil, 31077 Toulouse, France<sup>4</sup>Ioffe Physico-Technical Institute, Russian Academy of Sciences, 194021 St. Petersburg, Russia

(Received 23 April 2012; revised manuscript received 14 September 2012; published 19 November 2012)

We study in detail self-assembled (In,Ga)As quantum dots grown on GaP substrate from the structural, theoretical, and optical points of view. Single quantum dot morphology is first determined at the atomic level using plane-view scanning tunneling microscopy. Unusual  $C_2$  symmetry properties with high-index {136} facets are demonstrated for small quantum dots, whereas the apparent shape of the quantum dots approximately exhibits  $C_{2v}$  symmetry, with the appearance of low-index {111} facets when the quantum dot ripens. This is interpreted as a consequence of the competition between strain and surface energy during quantum dot formation. Electronic properties are then simulated using both  $\mathbf{k}\cdot\mathbf{p}$  and tight-binding models. The indium content and geometry of the quantum dots are found to have a strong influence on the transition type (direct-indirect). Finally, temperature-dependent optical properties of quantum dots are analyzed between 10 and 375 K. Photoluminescence and time-resolved photoluminescence studies show a clear proximity of two different types of optical transitions. Supported by the theoretical calculations, these transitions are interpreted as a competition between conduction band states in the  $X$  and  $\Gamma$  valleys.

DOI: [10.1103/PhysRevB.86.205316](https://doi.org/10.1103/PhysRevB.86.205316)

PACS number(s): 78.67.Hc, 68.37.Ef, 78.47.jd, 71.15.Ap

In recent years, the optoelectronic integrated circuits (OEIC) on silicon have become an important research topic, which is motivated by their great potentiality in information and communication technology.<sup>1</sup> The monolithic integration of lasers, based on III-V materials, and the compatibility with the current processing of electronic integrated circuits based on Si technology, remain the main stumbling block.<sup>2</sup> One of the most prominent issues comes from the large lattice mismatch existing between usual III-V materials (GaAs, InP) and Si, which leads to the formation of highly defective III-V layers with consequently poor optical properties.<sup>3</sup> This issue can be overcome by adopting a pseudomorphic approach, i.e. growing lattice-matched compounds on Si. Among binary III-V materials, GaP presents the closest lattice constant to Si (0.37% at 300 K). Moreover lattice matching can be obtained with the incorporation of 2% of nitrogen in GaP alloy. Recently, the epitaxial growth of GaP and GaPN<sub>0.02</sub> on Si substrate has been greatly improved by several groups.<sup>4-6</sup> However, GaP is not useful for most photonics applications due to its indirect band gap inducing a phonon-mediated light emission. As a direct band gap III-V material epitaxially grown on GaP is required, various materials and nanostructures have been proposed and tested. The approach that has obtained the best results is based on compressive strained GaNAsP/GaP quantum wells (QWs), for which electrically pumped laser was reported on GaP<sup>7</sup> (at room temperature) and on Si<sup>8</sup> (below 150 K). Another way consists of the elaboration of GaInPN/GaP QW-based light emitters.<sup>9</sup>

In parallel, quantum dots (QDs) have also been proposed as light emitter zones. They allow the coherent growth of smaller band gap material nanostructures with larger lattice mismatch. Furthermore, due to their 0D confinement properties, lower threshold currents have been demonstrated, in comparison to their QW counterparts.<sup>10</sup>

The (In,Ga)P/GaP QD system has been proposed. Gerhard *et al.*<sup>11</sup> have demonstrated high-density QDs of In-rich Ga<sub>0.46</sub>In<sub>0.54</sub>P on GaP (areal density  $\sim 1 \times 10^{11}$  cm<sup>-2</sup>). Low-intensity photoluminescence (PL) signal at 4 K was achieved. InP/GaP QDs have also been studied, and related devices have been developed.<sup>12</sup> However, band lineups between (In,Ga)P and GaP have been demonstrated to be borderline type I-type II, and the QD density was low ( $10^8$ - $10^9$  cm<sup>-2</sup>).<sup>13</sup>

The (In,Ga)As(N)/GaP QDs, with an appropriate In content, are expected to overcome the band lineups<sup>14</sup> issue. InAs/GaP QDs have first been proposed,<sup>15,16</sup> but efficient PL was not achieved because of the plastic relaxation due to the large lattice mismatch (11.2%). Then Shamirzaev *et al.*<sup>17</sup> have claimed the demonstration of type-I alignment for GaAs QDs on GaP, but strain relaxation processes and indirect band gap led to PL emission only up to 40 K. The room-temperature PL of InGaAsN/GaP QDs at 1.39 eV is the lowest emission energy that has ever been reported for any QD system on GaP.<sup>18</sup> However, the large full width at half-maximum (FWHM; 334 meV) was interpreted as a broad inhomogeneous distribution of the QDs. In a report on InGaAs/GaP QD properties, Fuchi *et al.*<sup>19</sup> have measured a PL signal up to 77 K and pointed out the issue of In composition. Calculations have been performed by Fukami *et al.*<sup>14</sup> showing the dominant role of In amount in the InGaAs(N)/GaP band lineups. Room-temperature PL was obtained in our group for a low In content.<sup>20</sup> Recently, Rivoire *et al.*<sup>21</sup> have claimed a single emission of type-I In<sub>0.5</sub>Ga<sub>0.5</sub>As/GaP QDs. Nevertheless, the issues of structural properties and alloy composition are not presented.

In this paper, we investigate structural, electronic, and optical properties of (In,Ga)As QDs. In the first section, samples' elaboration conditions are detailed. In Sec. II, structural properties are studied by atomic force microscopy (AFM)

and scanning tunneling microscopy (STM) at the atomic level. A theoretical study based on both tight-binding (TB) and  $\mathbf{k}\cdot\mathbf{p}$  simulations is described in Sec. III. This analysis is used to interpret the optical properties described in Sec. IV.

## I. EXPERIMENTS

(In,Ga)As QD samples devoted to AFM and STM measurements have been grown on n-doped GaP(001) substrates using a solid-source molecular beam epitaxy (MBE) apparatus. Substrate temperature was set to 580 °C, which is monitored by an optical pyrometer. A 500-nm-thick GaP buffer layer is first deposited, followed by a 3-monolayer (ML) (In,Ga)As deposition with a subsequent 30-s growth interruption under As. Nominal composition of indium was set to 30%. However, the effective indium composition depends upon indium segregation, indium desorption, or surface energies, which are nontrivial problems and require specific investigations.<sup>22</sup> Despite the desorption of In atoms, which arises when the temperature is higher than 520 °C, indium incorporation has been reported even at 595 °C during (In,Ga)As/GaAs deposition.<sup>23</sup> Moreover, the indium incorporation coefficient in InGaAs/GaAs epilayers at this temperature has been measured to be around 40–50%,<sup>24–27</sup> depending on growth conditions. Considering that the indium incorporation is dependent on the strain,<sup>25,28</sup> the indium incorporation coefficient in our case (i.e. on the GaP substrate) is even lower, which would lead to an indium effective composition below or equal to 15%.

For AFM measurements, the samples are then cooled down to room temperature. Atomic force microscopy is performed in contact mode. For STM studies, a 500-nm-thick GaP buffer layer is n-doped using silicon at  $10^{17}$  cm<sup>-3</sup>. It is followed by a 10-nm undoped GaP layer on which the QDs form. In this case, the samples are cooled down to 10 °C, and the amorphous As capping layers are deposited for 6 h with a beam equivalent pressure of  $5 \times 10^{-6}$  Torr. This amorphous capping layer prevents the nanostructures and the surface from any air contamination during the sample transfer<sup>29</sup> to the STM ultrahigh vacuum (UHV) chamber. The protective amorphous As layer is removed by heating the sample at 430 °C, which is monitored by the pyrometer. Electrochemically etched W STM tips were cleaned *in situ* by thermal heating before the STM experiments. Details of the experimental setup can be found elsewhere.<sup>30,31</sup> All STM experiments were performed at room temperature in the constant-current mode of operation. In the following, the tunnel voltage between tip and surface is noted  $U_t$  and tunnel current  $I_t$ . All images shown are filled-states images. Size and density of QDs on AFM and STM images were determined using Voronoi tessellation, adapted for particle counting of small QDs.<sup>32</sup>

For the analysis of optical properties (continuous-wave PL and time-resolved PL), (In,Ga)As QDs have been grown on n-doped GaP(001) substrate using a gas-source MBE apparatus. After the growth of a 450-nm buffer layer, and a 4-ML (In,Ga)As deposition with 30-s annealing under As (see Ref. 20 for more information), a 30-nm GaP capping layer is finally deposited to prevent surface nonradiative recombinations. Careful attention has been paid to ensure that

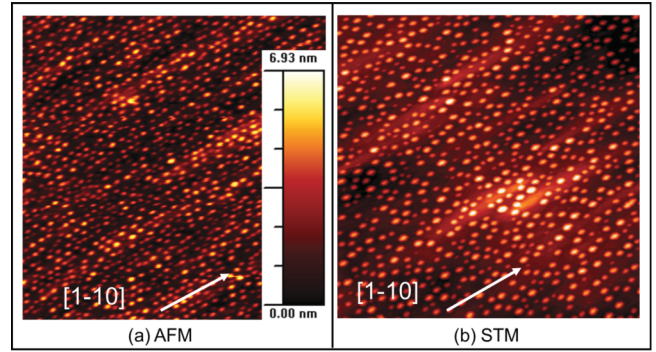


FIG. 1. (Color online) (a)  $800 \times 800$ -nm<sup>2</sup> AFM image of uncapped (In,Ga)As QDs, and (b)  $800 \times 800$ -nm<sup>2</sup> STM image ( $U_t = -3.27$  V;  $I_t = 0.04$  nA) of (In,Ga)As QDs, transferred to the STM chamber with amorphous As capping layer. The QD morphology has not changed during the transfer.

QDs grown in both MBEs give similar structural and optical properties.

## II. STRUCTURAL PROPERTIES

### A. AFM/STM comparison

In order to check whether the QDs remain unchanged during the amorphous As deposition and removal, and thus the validity of the STM measurements, preliminary experiments have to be conducted. Particularly, the QDs ripening during this stage should be avoided. For this purpose, structural properties have been first compared on two similar samples in Fig. 1. The first  $800 \times 800$ -nm<sup>2</sup> image [Fig. 1(a)] is directly obtained by AFM after the growth. The second one [Fig. 1(b)] is obtained by STM after amorphous As capping and decapping. The QD density is measured to be  $(1.5 \times 10^{11} \pm 0.2 \times 10^{11})$  cm<sup>-2</sup> in Fig. 1(a) and  $(1.3 \times 10^{11} \pm 0.2 \times 10^{11})$  cm<sup>-2</sup> in Fig. 1(b). A ripening of the QDs would clearly lower the QD density, which is not observed here.

Statistical analysis of heights and radii distributions was also performed. The mean QD height is equal to  $(3.0 \pm 1.0)$  nm in Fig. 1(a) and  $(3.5 \pm 1.2)$  nm in Fig. 1(b). The slight discrepancy may come from the underestimated height due to high QD density in the AFM scan. The measured mean radius is  $(11 \pm 2)$  nm in Fig. 1(a) and  $(9.0 \pm 1.8)$  nm in Fig. 1(b). This gives a typical aspect ratio (height-to-diameter ratio) of 0.2. The lateral extent of the QDs is thus measured to be different. This slight discrepancy can be mainly attributed to the convolution between real surface and tip, which is known to be more important in AFM than in STM. Accurate to within the uncertainty, the two sets of QD parameters can be considered identical. In conclusion, QD morphology is found to be the same before and after the amorphous As capping and decapping.

### B. Single QD morphology

Figure 2(a) presents a  $60 \times 60$ -nm<sup>2</sup> STM high-resolution image of the surface with a few QDs. Surface topography was derived to enhance contrast. Surface reconstruction of the planar areas allows us to unambiguously identify the

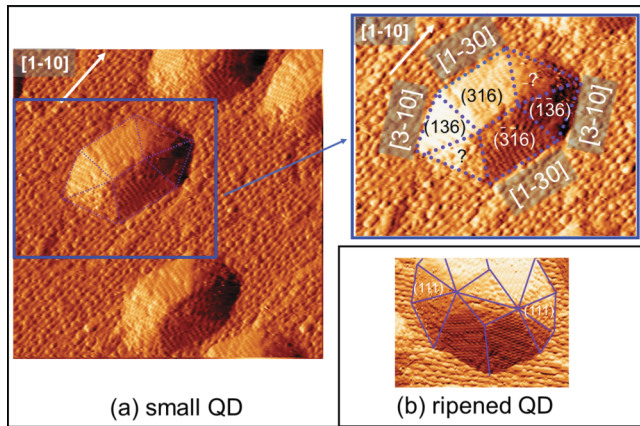


FIG. 2. (Color online) (a)  $60 \times 60\text{-nm}^2$  STM plane view ( $U_t = -2.87\text{ V}$ ;  $I_t = 0.01\text{ nA}$ ) of (In,Ga)As QDs not ripened. A detailed analysis of the image allows the identification of the facets in the inset. The symmetry of the crystal is not conserved in (b). The facet analysis for ripened QDs shows low-index facets appearing with underlying crystal symmetry.

$[1 - 1 0]$  crystallographic direction of the substrate. Atomic sites with high electronic density are observed on top of the QDs as well as on the base planar surface and are fingerprints of an indium-rich surface. Presence of indium reveals the existence of a wetting layer (WL), and thus demonstrates the Stranski–Krastanov (SK) growth mode of these QDs. Given the relatively low indium content in the structure due to the indium desorption at high-growth temperature ( $580^\circ\text{C}$ ), the (In,Ga)As alloy composition is thus likely inhomogeneous. It has been shown in the well-known (In,Ga)As/GaAs, (In,Al)As/GaAs, or (Ga,Al)As/GaAs systems that group-III elements with lower bond strength (i.e. indium here) tend to float on the growth surface, leading to the so-called In segregation.<sup>25,33–35</sup> This mechanism is expected to occur in our sample. In the extreme borderline case, the total amount of indium is located at the surface, and the QDs are exclusively composed of GaAs. In this situation, the predominant role of In in the QD nucleation is to increase the lattice mismatch and the QD nucleation driving force. The In-rich (In,Ga)As islands are expected to be precursors of the SK transition when the In concentration is high enough.<sup>36,37</sup> Actually, indium can be considered here as a catalyst for the GaAs QD nucleation.

Figure 2(a) inset presents the morphology of a typical small single QD, and Fig. 2(b) presents the morphology of a larger QD. The in-plane anisotropic ratio (between length and width) is reduced from 1.5 (small QD) to nearly 1 (large QD). These values show the relatively low in-plane anisotropy of our QDs. Facets were thus determined by measuring angles between facets and the base plane, combined with angle measurements between facet intersections with the base plane and the  $[1\bar{1}0]$  direction. Small QDs [Fig. 2(a)] exhibit six main facets, including (316), (136),  $(\bar{1}\bar{3}6)$ , and  $(\bar{3}\bar{1}6)$  well-defined planes, and two other facets with a more diffuse aspect; for these two facets, the dispersion on the measured angles is too large to conclude unambiguously. Directions of the QD edges under the (136) facets are  $[1 - 3 0]$  and  $[3 - 1 0]$ .

These high-index surfaces observed can be compared to other studies performed on In(Ga)As/GaAs QDs, where the stability of (137),<sup>38–42</sup> (136),<sup>43</sup> (125),<sup>44</sup> and even (2 5 11) planes,<sup>38,45</sup> were already discussed. In the case of InAs/InP (001) QDs, (136) facets were also observed.<sup>46</sup> Note that all the previously cited high-index planes are very close in the stereographic triangle;<sup>38</sup> the measurement accuracy does not allow to choose between these high-index planes [the (136) choice is the direct result of the angle measurement]. Our measurement confirms the thermodynamic stability of these high-index facets with the common InAs material system composing QDs on GaP, GaAs, and InP substrates. In the larger QD of Fig. 2(b), the QD presents additional facets, especially well-defined low-index (111) facets. Considering that large QDs are formed by the ripening process (increasing amount of atoms in the QD), this observation is in total agreement with observations performed on InAs/GaAs QDs.<sup>39,40</sup> This has also been observed in the SiGe materials system.<sup>47</sup> The energy gain  $E_{\text{tot}}$  associated with the formation of three-dimensional islands on the wetting layer is given by:<sup>39</sup>

$$E_{\text{tot}} = E_{\text{relax}} + E_{\text{surf}} + E_{\text{edge}}, \quad (1)$$

where  $E_{\text{relax}}$  is the contribution originating from bulk strain relaxation,  $E_{\text{surf}}$  the additional formation of facets, and  $E_{\text{edge}}$  the contribution of QD edge formation on the reconstructed surface. It is then shown that, considering a single QD at the thermodynamic equilibrium, its shape depends on its number of indium atoms. In accordance with our results, high-index facets are present for QDs with small number of atoms because the  $E_{\text{surf}}$  has a predominant role. Note that (136) and (316) planes are not reconstructed in the same way and thus do not have in this case the same energy. When the QD ripens, the increasing amount of atoms leads to the predominance of the  $E_{\text{relax}}$  contribution, which implies low-index facets, and to the increase of the number of facets. In Ref. 39, the third term  $E_{\text{edge}}$  is neglected because the detailed atomic structure near the edges is not known. This approximation is not valid for very small islands.

A striking feature of the QD is observed in the inset of Fig. 2(a): The QD does not have the  $\sigma_v$  plane symmetry that would be expected for conventional QDs. Indeed, a great deal of literature on the morphology of QDs report shape with at least a  $\sigma_{(1-10)}$  symmetry property and  $\sigma_{(110)}$  when grown on (001) substrate orientation [ $\sigma_{(abc)}$  refers here to the reflection through the (a b c) plane symmetry]. In the case of InAs/GaAs QDs grown on (001) substrate, the  $\sigma_{(1-10)}$  and  $\sigma_{(110)}$  have often been reported.<sup>38–41,43,44</sup> InAs/InP (001) quantum dashes also exhibit these two reflection planes.<sup>48</sup> The same symmetry properties  $\sigma_{(1-10)}$  and  $\sigma_{(110)}$  are also observed in II-VI QDs.<sup>49</sup> In all these cases, QDs are most of the time elongated along the  $[1 - 1 0]$  direction because of the velocity anisotropy of the adatoms diffusion at the reconstructed surface of the zinc-blende lattice. In the case of SiGe/Si (001) QDs, the situation is a bit different because of the Si diamond lattice. Quantum dots can be randomly elongated along the  $[1 - 1 0]$  or the  $[1 1 0]$  direction, or grown with a pyramidal shape.<sup>47,50</sup> Therefore, the nanostructures still keep their  $\sigma_{(1-10)}$  and  $\sigma_{(110)}$  plane symmetries. Even on the (113) substrate, QDs exhibit at least a  $\sigma_{(1-10)}$  symmetry, both on GaAs and InP.<sup>38,51,52</sup> In this case, the  $\sigma_{(110)}$  symmetry



is broken due to substrate orientation.<sup>53</sup> When growing nanostructures on (111) substrates, the  $\sigma_{(1-10)}$  QD symmetry is observed.<sup>54</sup> For QDs based on a wurtzite crystallographic structure, such as GaN/AlN, a triangular-like shape of the dots is reported.<sup>55</sup> The  $\sigma_{(1-10)}$  symmetry is always observed, while the  $\sigma_{(110)}$  symmetry does not exist because of the wurtzite lattice.

In most QD systems grown on (001) zinc-blende or diamond substrates, QD or quantum dash  $C_{2v}$ ,  $C_{3v}$ , or  $C_{4v}$  point symmetry is associated to a group-subgroup relationship with  $T_d$ ,  $C_{6v}$ , or  $O_h$  point groups.<sup>48,54</sup> In the present study, the (In,Ga)As/GaP QD exhibits a  $C_2$  symmetry (rotation of  $\pi$  around the [001] direction), but a  $C_{2v}$  symmetry is not observed, as the QD structure does not have vertical plane symmetry. A remarkable behavior lies in the fact that, in the particular case of ripened QDs [see Fig. 2(b)], even if the QDs remain  $C_2$  technically, numerous additional facets tend to introduce other symmetry properties. Especially, the presence of two additional facets on the top of the QD allows us to separate each (316) and ( $\bar{3}\bar{1}\bar{6}$ ) plane in two different facets. At the same time, the (136) or ( $\bar{1}\bar{3}\bar{6}$ ) and the undefined facet forms three different facets, including (111) planes, perpendicular to the [1 -1 0] direction. Additional facets are thus compatible with the  $\sigma_{(1-10)}$  symmetry property. The apparent shape of larger (ripened) QD approximately turns to  $C_{2v}$  symmetry.

Low-density InAs/InP(001) QDs grown by metalorganic vapor phase epitaxy (MOVPE)<sup>46</sup> are elongated toward [3-10] and [1-30] (similar to this work), with (136) facets. In this reference, the absence of characterization at the atomic scale does not allow to conclude accurately on the symmetry properties; although some of the observed QDs look very similar to that observed in this study. On the other hand, the dispersion on QD shape is very different. In Ref. 46, some QDs are diamond shaped, but most of them are slightly elongated, either in the [1-30] or in the [3-10] direction. Among the elongated islands, the proportion of QDs being elongated along one of these directions is claimed to be approximately 50%. For (In,Ga)As/GaP QDs, STM measurements clearly indicate that only one orientation exists [see Fig. 1(b)], likely because of the high density obtained during the growth. The work of Mano *et al.* on (In,Ga)As/GaAs QDs grown by MBE also presents some anisotropic QDs, elongated toward an undefined direction, which could correspond to a similar geometry.<sup>56</sup> In all three cases, InAs is deposited at a high-growth temperature ( $>530^\circ\text{C}$ ), and QDs with small sizes are obtained.

Considering the QD total energy, two contributions appear mainly: The bulk energy ( $E_{\text{relax}}$ ), and the surface contributions ( $E_{\text{surf}}$ ) and ( $E_{\text{edge}}$ ). While the bulk crystal of GaP follows the  $T_d$  point group symmetry, the presence of the free surface reduces this symmetry because of the electronic density surface reorganization. The reduced symmetry reached in this case depends on the kind of surface reconstruction. Considering that the three different contributions to the energy are the driving force for the QD nucleation, the appearance of additional  $\sigma_{(1-10)}$  facets confirms the increasing contribution of the bulk energy to the QD total energy during the QD ripening. Note that  $E_{\text{edge}}$  in this case cannot be neglected, given the small size of the (In,Ga)As/GaP QDs. This hypothesis requires

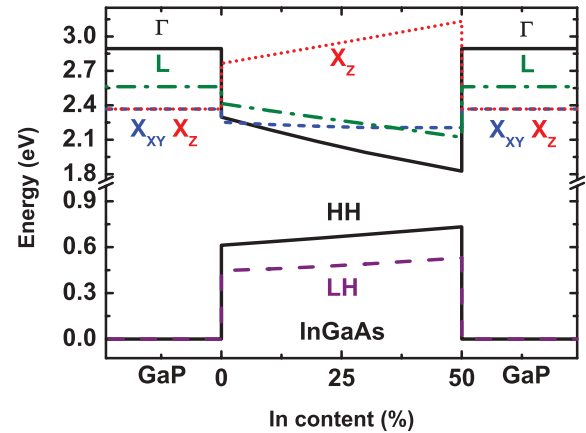


FIG. 3. (Color online) Band alignment and band structure of bulk  $\text{In}_x\text{Ga}_{1-x}\text{As}$  biaxially strained on GaP at 0 K.





detailed calculations at the atomic level, which are beyond the scope of this paper. The  $C_2$  QD symmetry is expected to have consequences on electronic and optical properties of single QD, for instance, through strain or piezoelectric effects.<sup>53,54</sup>

### III. BAND STRUCTURE CALCULATIONS

The knowledge of the electronic band structure of nanostructures is of crucial importance to understand their optical properties. First, we calculate the band structure of bulk InGaAs biaxially strained on GaP. For this purpose, we consider the extended-basis  $sp^3d^5s^*$  tight-binding model, which has proved to provide a band structure description throughout the entire Brillouin zone of binary semiconductors.<sup>57</sup> InGaAs ternary alloy is modeled by linear interpolations of all TB parameters but allows for a parabolic contribution of the relevant two-center parameters determining the experimental band positions at the  $\Gamma$ ,  $X$ , and  $L$  points. Strain effects are taken into account in the same way as smaller TB models.<sup>58</sup> The valence band offsets are taken from recent *ab initio* calculations.<sup>59</sup> The conduction and valence bands alignments are presented in Fig. 3 for an In content from 0% to 50%.

The valence band maximum in InGaAs unambiguously corresponds to the heavy-hole states because of the large compressive strain (3.7% for GaAs/GaP and 7.4% for  $\text{In}_{0.5}\text{Ga}_{0.5}\text{As}/\text{GaP}$ ). Thus, in the following, the heavy-hole state will be systematically considered as the valence band maximum. The case of the conduction band minimum is not so trivial. For low In content, the  $\Gamma$ ,  $L$ , and  $X_{XY}$  conduction band energies of InGaAs and the  $X$  conduction band energy of GaP are located in the same energy window of 150 meV. Thus, the lateral valleys are expected to have a strong influence on the band structure of InGaAs/GaP QDs. Nevertheless, handling the case of large QDs made of ternary alloys with atomistic methods is somewhat tricky. On the other hand, the eight-band  $\mathbf{k}\cdot\mathbf{p}$  method has been extensively used to calculate quantum levels in QDs with type-I band alignment and direct optical transition.<sup>60</sup> In this paper, we attempt to describe the band structure of our QDs by a combination of both methods:  $\mathbf{k}\cdot\mathbf{p}$  for the calculation of the first direct optical transition in QDs and TB for an estimation of the position of the first  $X$  and  $L$  energy

TABLE I. First electron and hole quantum levels in the  $\Gamma$  valley as a function of the shape of the QD keeping the height and the volume of the QD to constant values.

				
height (nm)	3.5	3.5	3.5	3.5
diameter at the base (nm)	18	16.8	15.2	10.4
HH (eV)	0.469	0.469	0.467	0.459
$\Gamma$ (eV)	2.397	2.384	2.371	2.358

levels. In Subsec. A, we describe the modeling strategy and justify the assumptions made for the calculations. In Subsec. B, results are presented.

### A. Modeling strategy

To calculate the direct optical transition, we consider the eight-band  $\mathbf{k}\cdot\mathbf{p}$  model. Scanning tunneling microscopy results of Sec. II have shown that QDs exhibit a small anisotropy. For simulation calculation, we thus consider a full  $C_{\infty v}$  symmetry and use a modified Hamiltonian for axial symmetry. This approximation has previously shown satisfactory results for the InAs/InP(100) QD system.<sup>53</sup> The strain calculation is performed by the finite element method. The shape of the QD is expected to have an influence on the strain distribution and thus on the band structure. In Table I, the first electron and hole quantum levels are reported for various shapes (cone, truncated cone, cylinder) keeping the height and the volume of the QD to constant values. The similarity of the results between the different shapes suggests that this influence is not so strong, and we have chosen to consider cone-shaped QDs in the following. The 3D-STM image of Fig. 4(a) is characteristic of the QD size dispersion. Four typical dimension sets are extracted from the figure and considered for the calculations. They are summarized in the table of Fig. 4(b). A typical wetting layer of 1 ML thick is added in the model to account for the Stranski–Krastanov growth mode. The direct transition energy is calculated for free electrons and holes. In this paper, neither exciton correction, piezoelectric effect, nor dielectric confinement effects are taken into account.<sup>61</sup> Deformation potentials and Luttinger parameters used in the  $\mathbf{k}\cdot\mathbf{p}$  are those extracted from the TB calculation for bulk InAs, GaAs, and GaP and are summarized in Table II.

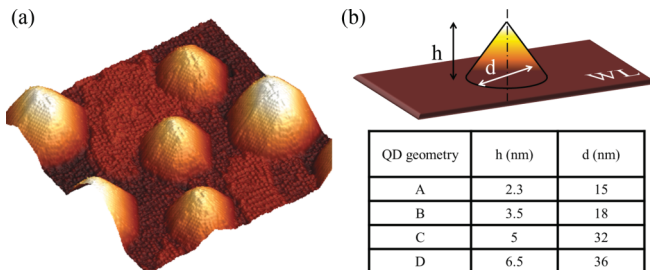


FIG. 4. (Color online) (a)  $75 \times 75$ -nm<sup>2</sup> STM 3D plane view of (In,Ga)As QDs showing the different size of QDs. (b) Cone-shaped QD geometry for the eight-band  $\mathbf{k}\cdot\mathbf{p}$  calculations.

TABLE II. Relevant material parameters used in the  $\mathbf{k}\cdot\mathbf{p}$  model.

	GaAs	InAs	GaP
$a_0$ (Å)	5.6533	6.0583	5.45
$C_{11}$ (GPa)	1211	832.9	1405
$C_{12}$ (GPa)	548	452.6	620.3
$C_{44}$ (GPa)	604	396	703.3
VBO (eV)	0.54	0.61	0
$a_c$ (eV)	-6.61	-4.89	-6.61
$a_v$ (eV)	1.73	1.35	1.91
$b$ (eV)	-1.91	-2.07	-1.79
$d$ (eV)	-4.8	-3.6	-4.6
$\gamma_1$	7.47	17.8	4.64
$\gamma_2$	2.16	7.69	0.73
$m_e$	0.067	0.024	0.139

To get an estimation of  $X$ - and  $L$ -state energies in the dot, we consider the TB model, but to avoid the need of a large supercell, we calculate the electronic levels in the  $X_{XY}$  and  $L$  conduction bands for a QW with a thickness equal to the height of the dot. Disregarding the lateral quantum confinement effect on these bands, we assume that the results are a good approximation of the  $X$ - and  $L$ -state energies for a QD. A justification is provided in Fig. 5. The first electronic levels in the  $\Gamma$ ,  $X_{XY}$ , and  $L$  valleys are calculated by the TB model for an In<sub>0.3</sub>Ga<sub>0.7</sub>As/GaP QW as a function of the thickness. It shows that quantum confinement mainly affects the  $\Gamma$  band. The  $X_{XY}$  and  $L$  are less affected because of their larger effective mass and their smaller conduction band offset with  $X$  and  $L$  bands of GaP (see Fig. 3). The transition associated with the wetting layer can also be simulated by a 1-ML-thick QW in TB description.

Another point has to be mentioned: Our calculation method assumes that the  $\Gamma$ ,  $X$ , and  $L$  levels in the dot can be calculated independently. Actually, the nature of the states in reciprocal space is not as well determined.<sup>61</sup> Indeed, due to the break of translational symmetry, complex band folding occurs in a QD Brillouin zone. Thus, electronic states originating from different points of the Brillouin zone of the parent bulk material

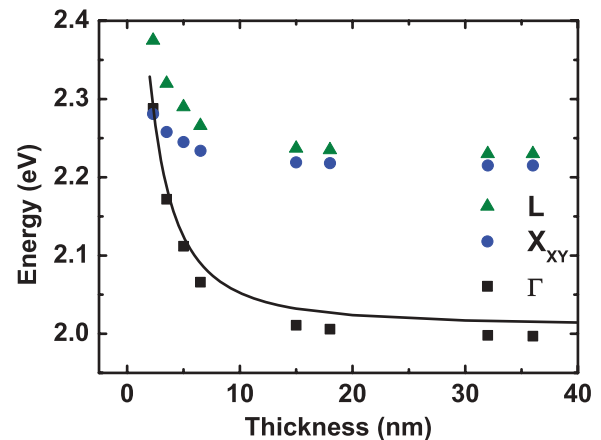


FIG. 5. (Color online) First electronic levels calculated in the  $\Gamma$ ,  $X_{XY}$ , and  $L$  valleys for an In<sub>0.3</sub>Ga<sub>0.7</sub>As/GaP QW as a function of the thickness by the TB model. The first electronic level in the  $\Gamma$  valley calculated by the  $\mathbf{k}\cdot\mathbf{p}$  method is shown by the solid line.

are mixed. This effect is more likely to occur when the states are close in energy. Thus, the states labeled  $\Gamma$  and  $X$  in our calculations should be coupled in a more advanced theoretical description. However, for the case of a QW, the  $\Gamma$  level can be calculated by both models; i.e. the eight- $\mathbf{k}\cdot\mathbf{p}$  method for which the conduction band mixing is not taken into account and TB model for which it is. The results of Fig. 5 show that both models give approximately the same value, suggesting that conduction band mixing has a negligible effect on the energetic position of the electronic levels.

### B. Results

The results for the four geometries are represented in Fig. 6. The case of the smaller QD (type A) is clear. The first  $\Gamma$ -like quantum confined electronic level (calculated by the  $\mathbf{k}\cdot\mathbf{p}$  method) lies well above the first  $X$  and  $L$  levels (calculated by the TB method). The energy separation between the  $X$  and the  $\Gamma$  level is found to be 400 and 240 meV for In contents of 0% and 30%, respectively. The  $X_{XY}$  and  $L$  states of GaP barrier material are even found to be at lower energy than the  $\Gamma$  level of the dot. The radiative emission from the  $\Gamma$ - $\Gamma$  transition is expected to be small for these dots. The case of the wetting layer is similar (not represented here). Due to the strong confinement effect, the  $\Gamma$  level of the WL lies above the  $X_{XY}$  and  $L$  states of both the WL and the GaP barriers. For type B QDs, the indirect-to-direct crossover occurs only for In content above 50%.

The cases of type C and type D QDs are somewhat different. Indeed, because of their higher dimensions, the

quantum confinement effect on the  $\Gamma$  conduction band is less pronounced. Thus, the lowest conduction band is found to be  $\Gamma$ -like for In content above 34% for C dots and above 29% for D dots. If we assume that there is about 15% of In in our QDs, the lowest conduction state is thus  $X$ -like. Nevertheless, for bigger dots, the  $\Gamma$  state lies 90 meV above the  $X$  state. Moreover, any effect of higher local In content or strain relaxation drives to a lowering of the  $\Gamma$  state and an indirect-to-direct transition can occur. The type-II transition (GaP  $X$  state with QD heavy-hole state) was presented as a limitation to InGaAs/GaP QD system because of the proximity of the first electron quantum level with the GaP  $X$  state.<sup>14</sup> Our present results show that the QD  $X$  state is actually the first limitation.

The energy of both first direct and first indirect ( $X$ - $\Gamma$ ) transitions for QDs of type C and D are represented on Fig. 7. Fukami *et al.*<sup>14</sup> have calculated the direct transition energy for InGaAs/GaP QDs in the In content range from 30% to 70%. Unlike in this paper, their calculations were performed at 300 K and for a square pyramid shape QD with a 4-nm height and a 20-nm width. Despite these differences, the calculated energies are in the same range of values. Song *et al.*<sup>63</sup> have reported PL of  $\text{In}_{0.5}\text{Ga}_{0.5}\text{As}/\text{GaP}$  QDs with a maximum of PL intensity between 1.88 and 2.00 eV. According to simulations, one should rather expect for an In content of 50% a first transition of direct type in the range of 1.5 eV. The discrepancy may be explained by the uncertainty on the composition of the QDs. Indeed, as quoted by the same authors,<sup>63</sup> a significant interdiffusion may alter

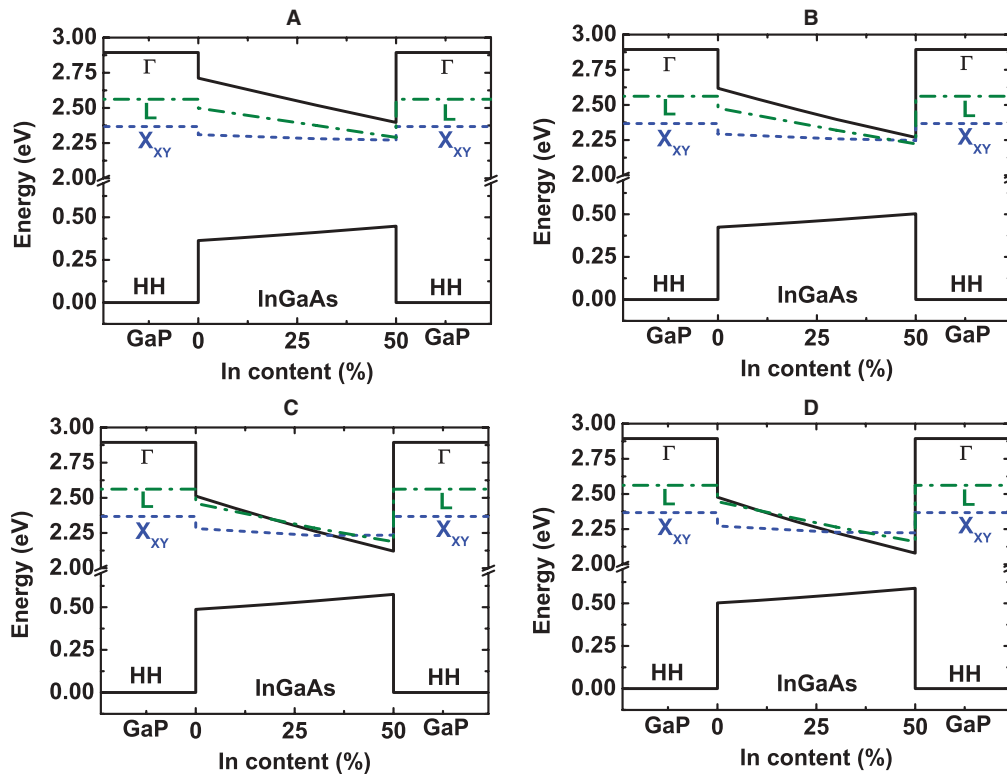


FIG. 6. (Color online) Band alignment and band structure of  $\text{In}_x\text{Ga}_{1-x}\text{As}$  QDs for the four geometries defined in Fig. 4(b). The first electronic level in the  $\Gamma$  valley and the first hole level are calculated by the  $\mathbf{k}\cdot\mathbf{p}$  method. The first electronic levels in the  $X$  and in the  $L$  valleys are calculated by the TB method. All calculations are performed at 0 K.

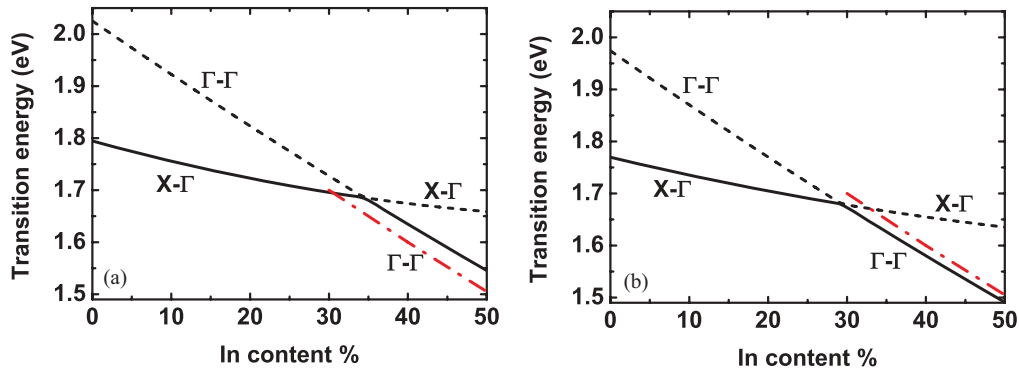


FIG. 7. (Color online) First direct transition energy and first indirect transition energy calculated for QD with (a) geometry C and (b) geometry D at 0 K. The red dash-dotted line shows the direct transition calculated by Fukami *et al.*<sup>14</sup> for a square pyramid shape with a 4-nm height and a 20-nm width at 300 K.

the composition of their QDs to  $\text{In}_x\text{Ga}_{1-x}\text{As}_{1-y}\text{P}_y$  with  $x < 0.5$  and  $y > 0$ . A lower-than-expected In content and a nonzero P incorporation may result in an increase of the band gap.

#### IV. OPTICAL PROPERTIES

##### A. Temperature-dependent PL

Photoluminescence experiments were carried out by exciting samples with a 405-nm continuous-wave laser diode. The power density is roughly estimated to be  $80 \text{ W cm}^{-2}$ . The samples were set in a helium bath closed-cycle cryostat to study PL from 10 K to room temperature. Measurements were also performed above room temperature using a hot plate. Attention was paid to avoid the red luminescence of the deep centers in n-doped GaP substrates. Actually, the penetration length of the 405-nm beam was lower than the thickness of the GaP buffer layer, avoiding the excitation of the substrate. Secondly, similar PL spectra were obtained on the same structures on nondoped GaP substrate, thus excluding any significant contribution from the GaP deep centers' luminescence.

Figure 8 presents PL spectra with the temperature varying from 12 to 375 K. The peak shape has a strong evolution from

low to high temperature. At 12 K, PL exhibits a single peak centered at 1.78 eV. It is, however, slightly power dependent and evolves to 1.76 eV at lower excitation power, as will be shown in the next section. The FWHM is equal to 97 meV and is attributed to the distribution of the dots' size. No signature of a wetting layer was found. A very high density of QDs may explain such behavior.<sup>64,65</sup> Moreover, as predicted in Sec. III, the confinement of the electrons in the  $\Gamma$  state of the wetting layer is unlikely because this state lies well above the X state of the GaP barrier. The temperature increase causes a classical red shift of the main peak to 1.74 eV at room temperature. At 260 K, a shoulder appears on the high-energy side of the spectrum. At 300 K, another optical transition clearly appears. When increasing the temperature above 300 K, the maximum of PL intensity switches from the low-energy (LE) transition to the higher-energy (HE) transition. A strong quenching of the maximum PL intensity is observed above 300 K because of the activation of nonradiative channels. The energies of both transitions have been extracted using a double Gaussian fitting. The results are shown for 300 K by thin red lines. The LE transition is found by fitting the low-energy side of the PL spectrum by a first Gaussian peak. The HE transition is found applying the same procedure on the spectrum, resulting from

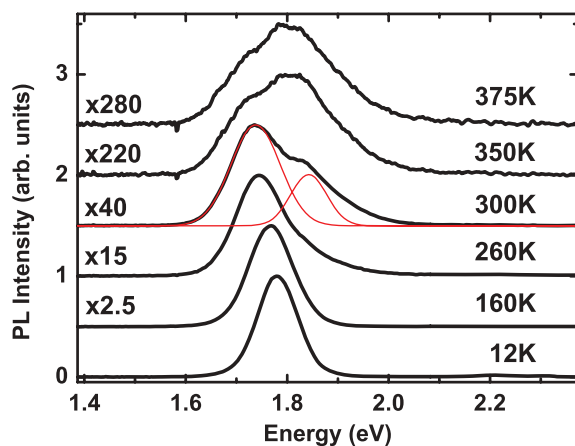


FIG. 8. (Color online) Temperature-dependent PL spectra of (In,Ga)As/GaP QDs. The red thin lines show the fit of the two transitions by two Gaussian peaks.

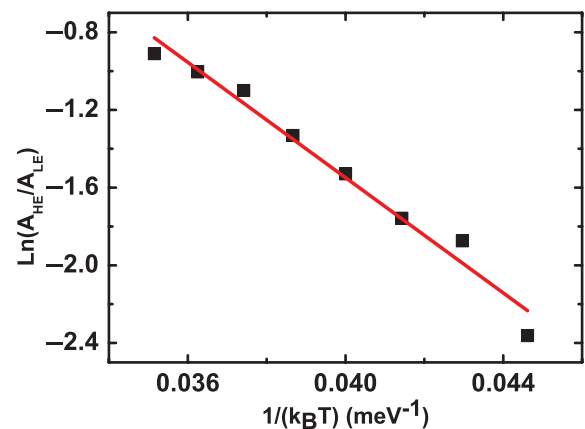


FIG. 9. (Color online) Ratio between the integrated intensities related to the two HE and LE transitions as a function of  $1/k_B T$ . The red line shows a linear fit.



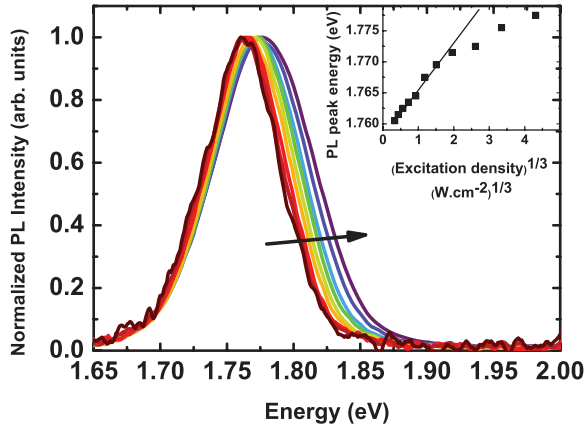


FIG. 10. (Color online) Normalized PL spectra as a function of excitation density at 12 K. The arrow represents the increasing of excitation density with the following values: 80, 180, 370, and 800  $\text{mW cm}^{-2}$ ; and 1.7, 3.4, 7.4, 17.8, 37, and 80  $\text{W cm}^{-2}$ . The insert shows the energy of the PL peak as a function of the cubic root of excitation density. The line is a guide to the eye.

the subtraction of the first Gaussian peak from the original PL spectrum. The rest of the high-energy tail is not fitted and is associated to the thermal filling of the highest energy states. The difference in energy between these two transitions is  $E_{\text{HE}} - E_{\text{LE}} = 100 \text{ meV}$ . The integrated intensity related to both transitions has been extracted by taking the areas under both Gaussians. In Fig. 9, the ratio between the integrated intensities of the HE transition ( $A_{\text{HE}}$ ) and the LE transition ( $A_{\text{LE}}$ ) is represented on a logarithm scale as a function of  $1/k_B T$ .

The linear shape of the curve is interpreted as the thermalization of electrons between both states with a ratio:

$$\frac{A_{\text{HE}}}{A_{\text{LE}}} = \frac{\tau_{\text{LE}}}{\tau_{\text{HE}}} \exp\left(-\frac{E_A}{k_B T}\right).$$

An activation energy  $E_A$  of  $140 \pm 10 \text{ meV}$  is deduced, which is consistent with the difference in energy between the two transitions  $E_{\text{HE}} - E_{\text{LE}}$ . The ratio  $\tau_{\text{LE}}/\tau_{\text{HE}}$  between the radiative lifetimes is found to be  $80 \pm 30$ , assuming that both states have the same degeneracy. It shows that the HE

optical transition is radiatively more efficient than the LE one.

This behavior can be interpreted on the basis of the theoretical results of Sec. III. The energy position of the LE PL peak at low temperature ( $E_{\text{LE}} = 1.76 \text{ eV}$ ) is consistent with the calculated indirect transition (between 1.74 and 1.79 eV for medium-sized dots in the 0% – 15% In content range. The  $E_{\text{HE}} - E_{\text{LE}}$  difference is also in reasonable agreement with theoretical calculations. For large-sized dots and In content of 15%, an energy difference of 100 meV was indeed calculated between both direct and indirect optical transitions (see Fig. 7). The limitations of the model are discussed in Sec. III. Moreover, the inhomogeneity in the alloy composition due to In segregation is not taken into account. Nevertheless, an assumption can be drawn for now: The LE PL peak at low temperature results from an indirect transition in QDs with In content below 15%. At room temperature, electrons get enough thermal energy to partially fill the  $\Gamma$  state, and thus a more efficient optical transition (HE) is observed. Excitation-dependent and time-resolved PL measurements will be presented in the following sections to provide additional insights.

### B. Excitation power-dependent PL

The variation of the excitation power is a commonly used technique to probe the excited states of QDs. Unfortunately, the experimental setup does not enable us to pump the sample with a power density larger than the one ( $80 \text{ W cm}^{-2}$ ) used in Sec. III-A. Figure 10 shows the normalized PL spectra at 12 K for excitation densities ranging from  $80 \text{ mW cm}^{-2}$  to  $80 \text{ W cm}^{-2}$ . The HE transition does not appear as a separate peak as it is the case at room temperature (Fig. 8). Nevertheless, increasing power density broadens the peak mainly on the high-energy side. It is related to the filling of the excited electron level in larger QDs. The energy position of the maximum PL intensity is also found to monotonously blue shift with the increase of the power density. Such behavior is often attributed to a type-II transition.<sup>66</sup> In that case, the position of the peak is expected to vary linearly with the excitation density to the power of 1/3. The corresponding curve plotted in the inset of Fig. 10 shows that data points clearly deviate from such a law

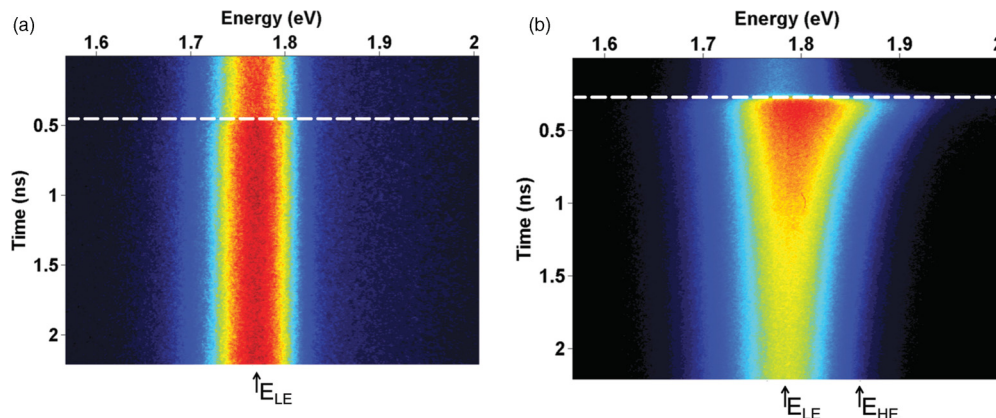


FIG. 11. (Color online) Streak camera image of time-resolved PL at 10 K for an excitation density of (a) LP =  $70 \text{ W cm}^{-2}$  and (b) HP =  $4000 \text{ W cm}^{-2}$ . The white horizontal dashed line marks the instant of the laser pulse.



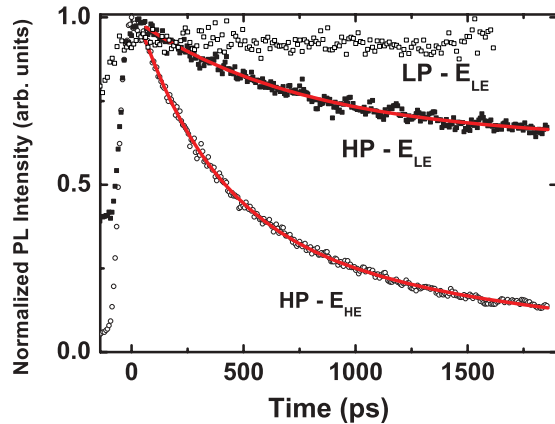


FIG. 12. (Color online) PL dynamics at selected energies ( $E_{LE} = 1.76$  eV and  $E_{HE} = 1.86$  eV) for two power densities (LP =  $70$  W  $\text{cm}^{-2}$  and HP =  $4000$  W  $\text{cm}^{-2}$ ). Red lines show biexponential fits.

above a low power of  $3$  W  $\text{cm}^{-2}$ . We thus believe that this energy shift is not due to a type-II transition but rather to HE transition occurring in larger QDs in agreement with the above discussion.

### C. Time-resolved PL

The dynamics of the recombination of carriers are investigated through time-resolved PL spectroscopy. The sample is excited by a frequency-doubled Ti:Sapphire laser at the wavelength of  $405$  nm. The repetition rate is  $80$  MHz. The PL signal is analyzed by a S20 streak camera, and measurements are performed at  $10$  K. The PL intensity variations on both wavelength and time are presented in Figs. 11(a) and 11(b) for two different excitation power densities. The estimated average excitation densities are respectively  $70$  W  $\text{cm}^{-2}$  for the low-power (LP) case and  $4000$  W  $\text{cm}^{-2}$  for the high-power (HP) case. When the QDs are excited with an LP density, the PL intensity exhibits a very long decay time independent of the emission energy, which is greater than the repetition period of the laser ( $12$  ns). This supports the interpretation in terms of an LE ground transition corresponding to an indirect-type transition. When the excitation density is increased [Fig. 11(b)], the PL spectrum broadens on the high-energy side as it was observed in Subsec. B. The decay time now depends on the emission energy with a shortening on the high-energy side.

The situation is more quantitatively detailed in Fig. 12. The time-resolved PL intensity is represented focusing on two detection energies:  $E_{LE} = 1.76$  eV and  $E_{HE} = 1.86$  eV. The energy positions are shown by arrows in Fig. 11. For the

LP case, the emission at  $E_{HE}$  is not detectable. For the HP case, the time-resolved emission related to the LE transition can be fitted by the sum of a short exponential decay with a lifetime of  $770$  ps and a constant associated with the very long lifetime of the indirect transition. The physical reason of the shortest time is more complex. It may be a result of many body effects such as Auger effects due to the high density of electron-hole pairs (above  $10$  per QD). For the HE transition, the emission shows a biexponential decay with short lifetimes of  $340$  and  $1700$  ps, respectively. Here again, many body effects and energy relaxation are expected to have an influence on the carriers dynamics.<sup>67</sup> Nevertheless, theoretical results presented in Sec. III B have shown that the calculated optical transition of direct type is consistent with the energy  $E_{HE}$ . This could be another reason for short decay times observed in these experiments.

## V. CONCLUSION

In conclusion, we have studied the (In,Ga)As/GaP QD system. Structural properties are analyzed by STM. The contribution to the QD formation energy is found to switch from surface to volume with the progressive ripening of the dot. This has consequences on the symmetry properties: Small dots exhibit high  $\{136\}$  index facets with a  $C_2$  symmetry, whereas low-index  $\{111\}$  facets are observed for larger dots. The band structure is then determined theoretically by a combination of  $\mathbf{k}\cdot\mathbf{p}$  and TB models for different QD geometries and as a function of In content. A ground transition of indirect type in reciprocal space is calculated for smaller dots or for low In content. For device applications, a ground transition of direct type is needed. Larger dots or a high enough In content are expected to fulfill this requisite. Optical properties of QDs in the low In content range are finally studied through temperature-, excitation-, and time-dependent PL. The results are consistent with a ground optical transition of indirect type. A second optical transition is present at room temperature, which could be of direct type, in agreement with theoretical calculations.

## ACKNOWLEDGMENTS

This research is supported by ‘‘Région Bretagne’’ through the PONANT project including FEDER funds. This work was performed using HPC resources from GENCI CINES and IDRIS 2012-c2012096724. The work is also supported through the participation of the SINPHONIC JC JC ANR project N° 2011 JS03006 and NANOTRANS C’NANO research program.

\*Corresponding author: cedric.robert@insa-rennes.fr

<sup>1</sup>M. J. Heck, H. W. Chen, A. W. Fang, B. R. Koch, Di Liang, Hyundai Park, M. N. Sysak, and J. E. Bowers, *IEEE J. Sel. Top. Quantum Electron.* **17**, 333 (2011).

<sup>2</sup>D. Liang and J. E. Bowers, *Nat. Photon.* **4**, 511 (2010).

<sup>3</sup>T. Egawa, Y. Murata, T. Jimbo, and M. Umeno, *IEEE Photonics Technol. Lett.* **9**, 872 (1997).

<sup>4</sup>K. Momose, H. Yonezu, Y. Fujimoto, Y. Furukawa, Y. Motomura, and K. Aiki, *Appl. Phys. Lett.* **79**, 4151 (2001).

- <sup>5</sup>K. Volz, A. Beyer, W. Witte, J. Ohlmann, I. Németh, B. Kunert, and W. Stolz, *J. Cryst. Growth* **315**, 37 (2011).
- <sup>6</sup>A. Létoublon, W. Guo, C. Cornet, A. Boulle, M. Véron, A. Bondi, O. Durand, T. Rohel, O. Dehaese, N. Chevalier, N. Bertru, and A. Le Corre, *J. Cryst. Growth* **323**, 409 (2011).
- <sup>7</sup>N. Hossain, S. J. Sweeney, S. Rogowsky, R. Ostendorf, J. Wagner, S. Liebich, M. Zimprich, K. Volz, B. Kunert, and W. Stolz, *Electron. Lett.* **47**, 931 (2011).
- <sup>8</sup>S. Liebich, M. Zimprich, A. Beyer, C. Lange, D. J. Franzbach, S. Chatterjee, N. Hossain, S. J. Sweeney, K. Volz, B. Kunert, and W. Stolz, *Appl. Phys. Lett.* **99**, 071109 (2011).
- <sup>9</sup>K. Umeno, S. M. Kim, Y. Furukawa, H. Yonezu, and A. Wakahara, *J. Cryst. Growth* **301-302**, 539 (2007).
- <sup>10</sup>N. N. Ledentsov, M. Grundmann, F. Heinrichsdorff, D. Bimberg, V. M. Ustinov, A. E. Zhukov, M. V. Maximov, Z. I. Alferov, and J. A. Lott, *IEEE J. Sel. Top. Quantum Electron.* **6**, 439 (2000).
- <sup>11</sup>S. Gerhard, V. Baumann, S. Höfling, and A. Forchel, *Nanotechnology* **20**, 434016 (2009).
- <sup>12</sup>F. Hatami, V. Lordi, J. S. Harris, H. Kostial, and W. T. Masselink, *J. Appl. Phys.* **97**, 096106 (2005).
- <sup>13</sup>F. Hatami, W. T. Masselink, L. Schrottke, J. W. Tomm, V. Talalaev, C. Kristukat, and A. R. Goñi, *Phys. Rev. B* **67**, 085306 (2003).
- <sup>14</sup>F. Fukami, K. Umeno, Y. Furukawa, N. Urakami, S. Mitsuyoshi, H. Okada, H. Yonezu, and A. Wakahara, *Phys. Status Solidi C* **8**, 322 (2011).
- <sup>15</sup>R. Leon, C. Lobo, T. P. Chin, J. M. Woodall, S. Fafard, S. Ruvimov, Z. Liliental-Weber, and M. A. Stevens Kalceff, *Appl. Phys. Lett.* **72**, 1356 (1998).
- <sup>16</sup>W. Guo, A. Bondi, C. Cornet, H. Folliot, A. Létoublon, S. Boyer-Richard, N. Chevalier, M. Gicquel, B. Alshawa, A. L. Corre, J. Even, O. Durand, and S. Loualiche, *Phys. Status Solidi C* **6**, 2207 (2009).
- <sup>17</sup>T. S. Shamirzaev, D. S. Abramkin, A. K. Gutakovskii, and M. A. Putyato, *Appl. Phys. Lett.* **97**, 023108 (2010).
- <sup>18</sup>K. Umeno, Y. Furukawa, N. Urakami, R. Noma, S. Mitsuyoshi, A. Wakahara, and H. Yonezu, *Physica E: Low-dimensional Systems and Nanostructures* **42**, 2772 (2010).
- <sup>19</sup>S. Fuchi, Y. Nonogaki, H. Moriya, A. Koizumi, Y. Fujiwara, and Y. Takeda, *Physica E: Low-dimensional Systems and Nanostructures* **21**, 36 (2004).
- <sup>20</sup>T. Nguyen Thanh, C. Robert, C. Cornet, M. Perrin, J. M. Jancu, N. Bertru, J. Even, N. Chevalier, H. Folliot, O. Durand, and A. Le Corre, *Appl. Phys. Lett.* **99**, 143123 (2011).
- <sup>21</sup>K. Rivoire, S. Buckley, Y. Song, M. L. Lee, and J. Vučković, *Phys. Rev. B* **85**, 045319 (2012).
- <sup>22</sup>A. D. Giddings, J. G. Keizer, M. Hara, G. J. Hamhuis, H. Yuasa, H. Fukuzawa, and P. M. Koenraad, *Phys. Rev. B* **83**, 205308 (2011).
- <sup>23</sup>S. C. Lee, L. R. Dawson, S. R. J. Brueck, and A. Stintz, *J. Appl. Phys.* **96**, 4856 (2004).
- <sup>24</sup>F. Fournier, R. A. Metzger, A. Doolittle, A. S. Brown, C. Carter-Coman, N. M. Jokerst, and R. Bicknell-Tassius, *J. Cryst. Growth* **175-176**, 203 (1997).
- <sup>25</sup>F. Turco and J. Massies, *Appl. Phys. Lett.* **51**, 1989 (1987).
- <sup>26</sup>J.-P. Reithmaier, H. Riechert, H. Schlöfberger, and G. Weimann, *J. Cryst. Growth* **111**, 407 (1991).
- <sup>27</sup>M. Mashita, Y. Hiyama, K. Arai, B.-H. Koo, and T. Yao, *Jpn. J. Appl. Phys.* **39**, 4435 (2000).
- <sup>28</sup>A. A. Mbaye, F. Turco, and J. Massies, *Phys. Rev. B* **37**, 10419 (1988).
- <sup>29</sup>N. Esser, U. Resch-Esser, M. Pristovsek, and W. Richter, *Phys. Rev. B* **53**, R13257 (1996).
- <sup>30</sup>S. Guézo, P. Turban, S. Di Matteo, P. Schieffer, S. Le Gall, B. Lépine, C. Lallaizon, and G. Jézéquel, *Phys. Rev. B* **81**, 085319 (2010).
- <sup>31</sup>S. Guézo, P. Turban, C. Lallaizon, J. C. Le Breton, P. Schieffer, B. Lépine, and G. Jézéquel, *Appl. Phys. Lett.* **93**, 172116 (2008).
- <sup>32</sup>C. Cornet, M. Hayne, P. Caroff, C. Levallois, L. Joulaud, E. Homeyer, C. Paranthoen, J. Even, C. Labbé, H. Folliot, V. V. Moshchalkov, and S. Loualiche, *Phys. Rev. B* **74**, 245315 (2006).
- <sup>33</sup>O. Dehaese, X. Wallart, and F. Mollot, *Appl. Phys. Lett.* **66**, 52 (1995).
- <sup>34</sup>J. Massies, F. Turco, A. Saletes, and J. P. Contour, *J. Cryst. Growth* **80**, 307 (1987).
- <sup>35</sup>Y. Iimura, K. Nagata, Y. Aoyagi, and S. Namba, *J. Cryst. Growth* **105**, 230 (1990).
- <sup>36</sup>A. G. Cullis, D. J. Norris, T. Walther, M. A. Migliorato, and M. Hopkinson, *Phys. Rev. B* **66**, 081305 (2002).
- <sup>37</sup>J. Tersoff and F. K. LeGoues, *Phys. Rev. Lett.* **72**, 3570 (1994).
- <sup>38</sup>K. Jacobi, *Prog. Surf. Sci.* **71**, 185 (2003).
- <sup>39</sup>P. Kratzer, Q. K. K. Liu, P. Acosta-Diaz, C. Manzano, G. Costantini, R. Songmuang, A. Rastelli, O. G. Schmidt, and K. Kern, *Phys. Rev. B* **73**, 205347 (2006).
- <sup>40</sup>G. Costantini, A. Rastelli, C. Manzano, P. Acosta-Diaz, R. Songmuang, G. Katsaros, O. G. Schmidt, and K. Kern, *Phys. Rev. Lett.* **96**, 226106 (2006).
- <sup>41</sup>J. Márquez, L. Geelhaar, and K. Jacobi, *Appl. Phys. Lett.* **78**, 2309 (2001).
- <sup>42</sup>P. Kratzer, A. Chakrabarti, Q. K. K. Liu, and M. Scheffler, *New J. Phys.* **11**, 073018 (2009).
- <sup>43</sup>H. Lee, R. Lowe-Webb, W. Yang, and P. C. Sercel, *Appl. Phys. Lett.* **72**, 812 (1998).
- <sup>44</sup>Y. Hasegawa, H. Kiyama, Q. K. Xue, and T. Sakurai, *Appl. Phys. Lett.* **72**, 2265 (1998).
- <sup>45</sup>L. Geelhaar, Y. Temko, J. Márquez, P. Kratzer, and K. Jacobi, *Phys. Rev. B* **65**, 155308 (2002).
- <sup>46</sup>A. Michon, I. Sagnes, G. Patriarche, G. Beaudoin, M. N. Mérat-Combes, and G. Saint-Girons, *Phys. Rev. B* **73**, 165321 (2006).
- <sup>47</sup>A. Rastelli, M. Stoffel, J. Tersoff, G. S. Kar, and O. G. Schmidt, *Phys. Rev. Lett.* **95**, 026103 (2005).
- <sup>48</sup>P. Miska, J. Even, C. Platz, B. Salem, T. Benyattou, C. Bru-Chévalier, G. Guillot, G. Bremond, K. Moumanis, F. H. Julien, O. Marty, C. Monat, and M. Gendry, *J. Appl. Phys.* **95**, 1074 (2004).
- <sup>49</sup>F. Tinjod, B. Gilles, S. Moehl, K. Kheng, and H. Mariette, *Appl. Phys. Lett.* **82**, 4340 (2003).
- <sup>50</sup>M. Stoffel, A. Rastelli, J. Tersoff, T. Merdzhanova, and O. G. Schmidt, *Phys. Rev. B* **74**, 155326 (2006).
- <sup>51</sup>Y. Temko, T. Suzuki, P. Kratzer, and K. Jacobi, *Phys. Rev. B* **68**, 165310 (2003).
- <sup>52</sup>D. Lacombe, A. Ponchet, S. Fréchengues, V. Drouot, N. Bertru, B. Lambert, and A. Le Corre, *Appl. Phys. Lett.* **74**, 1680 (1999).
- <sup>53</sup>C. Cornet, A. Schliwa, J. Even, F. Doré, C. Celebi, A. Létoublon, E. Macé, C. Paranthoen, A. Simon, P. M. Koenraad, N. Bertru, D. Bimberg, and S. Loualiche, *Phys. Rev. B* **74**, 035312 (2006).
- <sup>54</sup>K. F. Karlsson, M. A. Dupertuis, D. Y. Oberli, E. Pelucchi, A. Rudra, P. O. Holtz, and E. Kapon, *Phys. Rev. B* **81**, 161307 (2010).
- <sup>55</sup>S. Founta, C. Bougerol, H. Mariette, B. Daudin, and P. Vennéguès, *J. Appl. Phys.* **102**, 074304 (2007).
- <sup>56</sup>T. Mano, R. Nötzel, G. J. Hamhuis, T. J. Eijkemans, and J. H. Wolter, *J. Cryst. Growth* **251**, 264 (2003).

- <sup>57</sup>J.-M. Jancu, R. Scholz, F. Beltram, and F. Bassani, *Phys. Rev. B* **57**, 6493 (1998).
- <sup>58</sup>P. Boring, J. M. Jancu, B. Gil, D. Bertho, C. Jouanin, and K. J. Moore, *Phys. Rev. B* **46**, 4764 (1992).
- <sup>59</sup>Y. H. Li, A. Walsh, S. Chen, W. J. Yin, J. H. Yang, J. Li, J. L. F. Da Silva, X. G. Gong, and S. H. Wei, *Appl. Phys. Lett.* **94**, 212109 (2009).
- <sup>60</sup>O. Stier, M. Grundmann, and D. Bimberg, *Phys. Rev. B* **59**, 5688 (1999).
- <sup>61</sup>M. Mosko, D. Munzar, and P. Vagner, *Phys. Rev. B* **55**, 15416 (1997).
- <sup>62</sup>A. J. Williamson, A. Franceschetti, H. Fu, L. W. Wang, and A. Zunger, *J. Electron. Mater.* **28**, 414 (1999).
- <sup>63</sup>Y. Song, P. J. Simmonds, and M. L. Lee, *Appl. Phys. Lett.* **97**, 223110 (2010).
- <sup>64</sup>L. Landin, M. Borgström, M. Kleverman, M. E. Pistol, L. Samuelson, W. Seifert, and X. Zhang, *Thin Solid Films* **364**, 161 (2000).
- <sup>65</sup>S. Hinooda, S. Loualiche, B. Lambert, N. Bertru, M. Paillard, X. Marie, and T. Amand, *Appl. Phys. Lett.* **78**, 3052 (2001).
- <sup>66</sup>M. K. K. Nakaema, F. Iikawa, M. J. S. P. Brasil, E. Ribeiro, G. Medeiros-Ribeiro, W. Carvalho, M. Z. Maialle, and M. H. Degani, *Appl. Phys. Lett.* **81**, 2743 (2002).
- <sup>67</sup>C. Cornet, C. Labbé, H. Folliot, P. Caroff, C. Levallois, O. Dehaese, J. Even, A. Le Corre, and S. Loualiche, *Appl. Phys. Lett.* **88**, 171502 (2006).